



Research paper

A novel $\text{Ag}_2\text{O}/\text{CeO}_2$ heterojunction photocatalysts for photocatalytic degradation of enrofloxacin: possible degradation pathways, mineralization activity and an in depth mechanism insight



Xiao-Ju Wen, Cheng-Gang Niu*, Lei Zhang, Chao Liang, Guang-Ming Zeng

College of Environmental Science Engineering, Key Laboratory of Environmental Biology Pollution Control, Ministry of Education, Hunan University, Changsha 410082, China

ARTICLE INFO

Keywords:
 CeO_2
 Ag_2O
 Visible light
 $p\text{-}n$ heterojunction
 Enrofloxacin

ABSTRACT

Semiconductor photocatalysis has been considered as one of the most promising technologies for the removal of antibiotics from aqueous solutions. In this study, $\text{Ag}_2\text{O}/\text{CeO}_2$ $p\text{-}n$ heterojunction photocatalysts were fabricated by an *in situ* loading Ag_2CO_3 on CeO_2 spindles and subsequent via a thermal decomposition process. The $\text{Ag}_2\text{O}/\text{CeO}_2$ composites exhibited enhanced photocatalytic activity for the photodegradation of enrofloxacin (EFA) under visible light irradiation. A plausible degradation pathway for EFA was proposed. The $\text{Ag}_2\text{O}/\text{CeO}_2$ heterojunction photocatalysts exhibited the high mineralization ability towards the EFA molecule degradation based on three-dimensional excitation–emission matrix fluorescence spectroscopy (3D EEMs) and total organic carbon (TOC) analysis. Transient photocurrent response, PL spectrum and EIS indicate high photoinduced charge separation efficiency possess in $\text{Ag}_2\text{O}/\text{CeO}_2$ composites. Active species trapping experiments and ESR technique confirmed that h^+ and $\cdot\text{O}_2$ were the main active groups involved in photo-degradation of organic pollutants. Through the combination of various performance characterization and experimental results, a possible photocatalytic mechanism was proposed. Moreover, the energy band alignments of $\text{Ag}_2\text{O}/\text{CeO}_2$ heterostructure were calculated, which provided strong support for the proposed mechanism. This work could provide a new approach to construct new heterojunction photocatalysts and a deeper insight for the heterojunction catalyst.

1. Introduction

The widespread usage of antibiotics has received the increasing concern in recent years due to the enormous amounts residuals in aquatic environments. Enrofloxacin (EFA), a common Fluoroquinolones (FQs) antibiotic, is extensively used in human and veterinary medicine [1]. Frustratingly, a majority of EFA was eventually discharged into aquatic environments since only partially metabolism in human or animal body and poor biodegradability [2]. The presence of EFA in water even at trace level, would damage human health and aquatic ecosystems [3]. It has been listed as an important priority contaminant in many countries. However, traditional wastewater treatment plants would not eliminate it effectively. In this case, various methods have been exploited to disposal of it, such as advanced oxidation treatment [4], photoelectron-Fenton [5] and electrochemical treatments [6]. Unfortunately, most of these methods require the utilization of unstable and costly oxidants. Also some secondary pollutants are easy to be formed during degradation processes [7]. Therefore, it is still highly desired to seek an efficient, environmentally friendly approach to

remove EFA from waters.

Semiconductor photocatalysis has been considered as one of the most promising technologies for the removal of antibiotics from aqueous solutions due to their low-cost and eco-friendly approaches [8,9]. However, traditional photocatalyst TiO_2 only can utilize UV light to degrade organic pollutants, which largely limited its practical application [10]. Researchers have been looking for new visible light driven (VLD) photocatalysts to replace it. After the research of past few decades, a variety of visible light driven catalysts were reported, such as C_3N_4 [11], BiVO_4 [12], Ag_3PO_4 [13] and etc. In terms of various visible light driven photocatalysts, many of them also suffer from some disadvantages, such as limited light absorption capacity, rapid recombination of electron holes and poor stability. Therefore, it is still imminent for exploiting new photocatalysts with highly efficient visible light driven and fast charge carrier's separation.

Among the emerging catalysts, *n*-type semiconductor Ceria (CeO_2) was considered to be one of the promising catalyst materials owing to its high catalyst activity, low cost and environmentally friendly properties [14–16]. Unfortunately, its catalytic activity is still poor due to

* Corresponding author.

E-mail addresses: wenxiaoju1990@126.com (X.-J. Wen), cgniu@hnu.edu.cn, cgniu@hotmail.com (C.-G. Niu).

fast recombination of photoinduced electron-hole pairs and limited visible light adsorption capacity. In recent years, various strategies, such as controlling morphologies [17], doping metals [18], and fabricating heterojunctions, [19] have been employed to overcome these drawbacks. For instance, Xu et al. was successfully prepared yttrium-doped hedgehog-like ceria with a high photocatalytic activity by a traditional hydrothermal process [20]. In the case of various strategies, fabricating CeO_2 -based heterojunction photocatalysts have been proven the most convenient way to improve the photocatalytic performance of ceria, which can not only prominently enhance light absorption ability but also promote charge separation and transfer effectively due to their proper band-gap position and valid heterojunction [21,22]. Among, the fabrication of CeO_2 -based *p-n* heterojunction may be a good choice [23]. Recently, Wen et al. have reported CeO_2/BiOX ($X = \text{Br, I}$) *n-p* heterojunction displayed excellent photocatalytic performance towards pollutants degradation under visible light [24,25]. It can be perceived that construction of CeO_2 -based *p-n* heterojunction may be a good strategy for exploiting new visible light driven photocatalyst.

Ag_2O , an attractive *p*-type VLD semiconductor, has the strong absorption in the visible light region [26]. However, single Ag_2O still exhibits poor photocatalytic activity due to low quantum yield, poor light stability and short life of charge carriers. In order to improve its photocatalytic performance, constructing Ag_2O -based *p-n* heterojunctions has been considered a good strategy, which can not only improve the life of photogenerated charge carriers, but also can improve its light stability [27,28]. Liang et al. have demonstrated the photocatalytic performance of $\text{Bi}_2\text{O}_2\text{CO}_3$ can be greatly enhanced by fabricating *p-n* junction with Ag_2O [29]. Very recently, Li and coworkers developed $\text{Ag}_2\text{O}/\text{TaON}$ and $\text{Ag}_2\text{O}/\text{Ta}_3\text{N}_5$ *p-n* heterojunctions photocatalysts and they present noteworthy photoactivity for the degradation of organic pollutants with irradiation of visible light [30,31]. Inspired by these researches, we intend to load Ag_2O nanoparticles on surface of CeO_2 for constructing a *p-n* junction. On the one hand, it can greatly improve the visible light absorption capacity of CeO_2 ; on the other sides, light stability of the Ag_2O and the separation of photogenerated charge carriers can also be promoted greatly. Therefore, it is appealing and highly anticipated for the construction of $\text{Ag}_2\text{O}/\text{CeO}_2$ *p-n* heterojunction.

Herein, CeO_2 was firstly prepared via urea hydrolysis and calcination. $\text{Ag}_2\text{O}/\text{CeO}_2$ *p-n* heterojunction photocatalysts were synthesized by thermal decomposition process. The photocatalytic activity of the obtained photocatalyst was evaluated via the photodegradation of EFA under visible light irradiation. A plausible degradation pathway for EFA was also proposed according to LC-MS analysis. Three-dimensional excitation–emission matrix fluorescence spectroscopy (3D EEMs) and TOC were used to further evaluate the mineralization ability of the $\text{Ag}_2\text{O}/\text{CeO}_2$ composites towards the EFA degradation. The charge separation and migration behaviors of the as-fabricated samples were evacuated via photoluminescence (PL), electrochemical impedance spectroscopy (EIS) and photocurrent tests. Mott-Schottky tests (MS) were applied to confirm flat band potential and semiconductors types of the pure CeO_2 and Ag_2O . The active species trapping experiments and the electron spin resonance (ESR) technique were conducted for identifying reactive species participated in the photocatalytic degradation process. Ultimately, a plausible mechanism was also proposed in detail. Furthermore, the energy band alignments of $\text{Ag}_2\text{O}/\text{CeO}_2$ heterostructure were calculated to provide the evidence for the proposed mechanism.

2. Experimental

2.1. Chemicals and reagents

Cerium nitrate hexahydrate ($\text{Ce}(\text{NO}_3)_6 \cdot 6\text{H}_2\text{O}$), polyvinylpyrrolidone K30 (PVP), silver nitrate (AgNO_3), sodium dodecylbenzene sulfonate (SDBS), isopropyl alcohol (IPA), sodium oxalate ($\text{Na}_2\text{C}_2\text{O}_4$), benzoquinone (BQ), enrofloxacin (EFA), sodium bicarbonate (NaHCO_3) and Urea

were all purchased from Shanghai chemical Reagents Co., Ltd. All ultrapure water used in all the experiments was obtained from a Milli-Q ultrapure (18.25 $\text{M}\Omega \text{ cm}$) system.

2.2. Synthesis of CeO_2

CeO_2 were prepared via urea hydrolysis and calcination according to following procedure. 1.0 g PVP and 27.0 g of urea were added to 100 mL of 0.10 mol/L $\text{Ce}(\text{NO}_3)_6$ aqueous solution, the mixture was stirred at 85 °C for 2 h. Then the white powder was obtained through vacuum filtration, washed and dried. Finally, the white precipitates were calcined at 400 °C for 2 h with a heating rate of 5 °C/min.

2.3. Fabrication of $\text{Ag}_2\text{CO}_3/\text{CeO}_2$ photocatalyst

$\text{Ag}_2\text{CO}_3/\text{CeO}_2$ photocatalysts were fabricated using a facile in-situ coprecipitation method with assistant of SDBS. In brief, 0.20 g CeO_2 and 0.1 g SDBS were ultrasonically dispersed in 60 mL of distilled water to get a uniform solution A. Then 6.0 mL 0.10 M silver nitrate solution was added dropwise to the solution A under vigorous stirring. The mixture was further stirred for 30 min at room temperature. Afterwards, 6.0 mL 0.10 M NaHCO_3 solution was added dropwise the above solution and stirred for 4 h in dark. Eventually, the precipitates were collected by vacuum filtration and washed several times with ultrapure water and alcohol. The $\text{Ag}_2\text{CO}_3/\text{CeO}_2$ composites with 29.28 wt% of Ag_2CO_3 mass ratios (denoted as ACC-3) were obtained after dried in a vacuum oven at 60 °C for 12 h. Similarity, by changing the volume of AgNO_3 (2.00 mL, 4.00 mL, 6.00 mL, 8.00 mL), $\text{Ag}_2\text{CO}_3/\text{CeO}_2$ composites with different Ag_2CO_3 mass ratios of 12.13 wt%, 21.63 wt%, 35.57 wt% (denoted as ACC-1, ACC-2 and ACC-4) were obtained, respectively.

2.4. Fabrication of $\text{Ag}_2\text{O}/\text{CeO}_2$ photocatalyst

$\text{Ag}_2\text{O}/\text{CeO}_2$ *p-n* heterojunction photocatalysts were synthesized by thermal decomposition of the as-synthesized $\text{Ag}_2\text{CO}_3/\text{CeO}_2$. In brief, the as-synthesized $\text{Ag}_2\text{CO}_3/\text{CeO}_2$ sample was placed into an open crucible and heated to 220 °C for 2 h with a heating rate of 5 °C/min. The as-prepared ACC-1, ACC-2, ACC-3 and ACC-4 composites were calcinated according the same process. After calcination, they were denoted as AOC-1 (with Ag_2O mass ratios of 10.29 wt%), AOC-2 (with Ag_2O mass ratios of 18.83 wt%), AOC-3 (with Ag_2O mass ratios of 25.82 wt%) and AOC-4 (with Ag_2O mass ratios of 31.69 wt%), respectively. The pure Ag_2O was prepared according to the same procedure as above through the calcination of Ag_2CO_3 .

2.5. Characterization

X-ray diffraction (XRD) patterns were recorded on a Bruker D8 Advance instrument in 2θ range of 10–80°. The morphologies were examined with a Zeiss Supra 55 field-emission scanning electron microscope (SEM). X-ray photoelectron spectroscopy (XPS) was performed on a Thermo ESCALAB 250X. UV-vis diffuse reflectance spectra (DRS) were measured on Hitachi U-4100 using with BaSO_4 as a reference material. Fluorescence spectra were monitored with a fluorescence spectrophotometer. Three-dimensional excitation–emission matrix fluorescence spectroscopy (3D EMMs) and the PL spectra were recorded on FluoroMax-4 fluorescence spectrophotometer. Shimadzu Total Organic Analyzer (TOC-L series) was used to perform TOC analysis. ICP was conducted on an Agilent ICPOES730. The electron spin response (ESR) signals of radicals spin-trapped by spin-trapped reagent 5, 5-dimethyl-L-pyrroline N-oxide (DMPO) were examined on a Bruker E500 spectrometer under visible light irradiation ($\lambda > 420 \text{ nm}$). Electrochemical measurements were carried out via a CHI660E electrochemical workstation with a standard three-electrode. The details were provided in Supplementary Information.

2.6. Photocatalytic activity tests

EFA was used to evaluate the photocatalytic activities of the obtained samples. The visible light was emitted through a 300 W Xe lamp (Zhong jiao jin yuan, CEL-HXF300) equipped with a UV Cut-off filter (UVCUT420). Briefly, 50 mg catalyst was added into EFA (50 mL, 10 mg/L) solutions. Before switched on the light, the suspensions were stirred 30 min in the dark to reach adsorption-desorption equilibrium. In the photodegradation process, an approximately 3.0 mL suspension was taken out and separated at given time intervals to obtain the supernatant liquids. The concentration of the pollutants was measured with a UV-vis spectrophotometer at their maximum absorption wavelength (277 nm for EFA). Determination of the photodegradation intermediates of EFA was carried out on a LC-MS system. The details were provided in Supplementary Information.

3. Results and discussion

3.1. Characterization of the obtained samples

X-ray diffraction (XRD) was implemented to investigate the crystal structures and phase purities of CeO_2 , Ag_2O and AOC-3 composites. The results were depicted in Fig. 1. For pure CeO_2 , the main diffraction peaks at 2 θ values of 28.53°, 33.01°, 47.44°, 56.34°, 59.01°, 69.41°, 76.70° and 79.05° can be observed, which relate well with the (1 1 1), (2 0 0), (2 2 0), (3 1 1), (2 2 2), (4 0 0), (3 3 1) and (4 2 0) planes of the cubic fluorite structured CeO_2 crystal (JCPDS Card No:43-1002) [32]. Besides, no additional crystal phases are observed, implying the as-synthesized CeO_2 is unadulterated. In the XRD pattern of pure Ag_2O , the diffraction peaks at 26.73°, 32.90°, 38.28°, 55.16°, 65.70° and 68.92° can be indexed to the (1 1 0), (1 1 1), (2 0 0), (2 2 0), (3 3 1) and (2 2 2) planes of the cubic phase of Ag_2O (JCPDS Card No: 65-6811) [33]. With respect to the AOC-3 samples, the typical diffraction peaks of CeO_2 and Ag_2O could be observed obviously. Some peaks of Ag_2O are not obvious and weak, which is probably attributed to the low content of Ag_2O and shading effect of the CeO_2 . The above results demonstrate that the $\text{Ag}_2\text{O}/\text{CeO}_2$ composites are obtained, and the crystalline phase of CeO_2 is not severely affected after the loading of Ag_2O .

The morphology and size of the as-prepared samples were characterized using SEM (Fig. 2). From the images in Fig. 2a,b, it can observe that the pristine CeO_2 reveals a spindles structure. After decorating with Ag_2O , it can clearly see that Ag_2O nanoparticles anchored on the surface of CeO_2 intimately, which is conducive to the formation of heterojunction between CeO_2 and Ag_2O . Moreover, TEM instrument

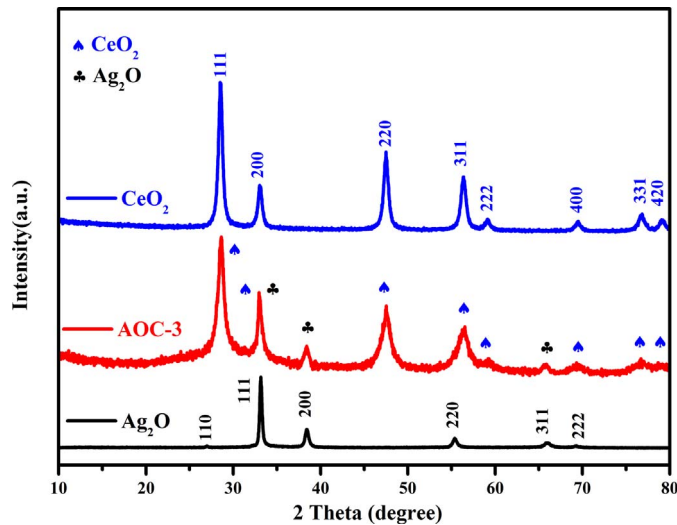


Fig. 1. XRD patterns of CeO_2 , Ag_2O and AOC-3 composites.

was used to further confirm the heterojunction in $\text{Ag}_2\text{O}/\text{CeO}_2$ composites. From Fig. 2e, it can be seen that some spherical nanoparticles are formed on the surface of CeO_2 . As for Fig. 2f, it is clear that the interplanar distances 0.312 nm and 0.191 nm corresponding to the (1 1 1) and (2 0 0) plane of CeO_2 respectively. The spacing with 0.274 and 0.236 nm correlated with the (1 1 1) and (2 0 0) plane of Ag_2O . Moreover, the distinct interface between CeO_2 and Ag_2O would contribute to the separation of the photo-excited charge carriers. On the basis of the above results, it can be inferred that $\text{Ag}_2\text{O}/\text{CeO}_2$ heterojunction photocatalysts have been successfully prepared.

Additionally, SEM-EDS technique was performed to reveal the elemental distribution of the AOC-3 composite. Fig. 3 presented the SEM image and corresponding element mapping images. As presented in Fig. 3, the elements of Ce, O and Ag distributed uniformly within the composites, suggesting that the Ag_2O are successfully loaded on the surface of CeO_2 . Besides, the EDX spectrum of the AOC-3 composite (Fig. 3e) further proved the presence of Ce, O, and Ag within the composites.

The surface elemental composition and the chemical states of CeO_2 , Ag_2O and AOC-3 composites were investigated by XPS. The survey spectra in Fig. 4a displayed that the CeO_2 and Ag_2O contain Ce, O and Ag, respectively; while Ce, Ag and O can be observed in the survey XPS spectrum of AOC-3, implying CeO_2 and Ag_2O coexist in the AOC-3 composites. In the Ce 3d level (Fig. 4b), six peaks can be observed, the peaks at 882.16 eV, 888.65 eV, and 898.14 eV were assigned to Ce 3d_{5/2}, and the peaks centered at 900.63 eV, 907.15 eV, and 916.54 eV were ascribed to Ce 3d_{3/2}, indicating the main Ce^{4+} chemical valence in hybrids [34]. The Ag 3d peaks at 368.10 eV and 374.22 eV can be separately attributed to the Ag 3d_{5/2} and Ag 3d_{3/2} of Ag^+ [24]. Meanwhile, two peaks can be observed in the O 1 s spectrum (Fig. 4d). The peak at 529.21 eV is indexed to the Ce-O bond and Ag-O. And the other peak is related to adsorbed oxygen and H_2O [35]. Further, the Ce 3d, Ag 3d and O 1 s core level peaks of the AOC-3 show a shift after introducing Ag_2O , indicating that the chemical environment has been changed. The results of the XPS analysis illustrated Ag_2O linked with CeO_2 via chemically bound interface rather than a physical contact.

To inspect the optical absorption properties of CeO_2 , Ag_2O and $\text{Ag}_2\text{O}/\text{CeO}_2$ composites, UV-vis diffuse reflection spectroscopy technique was used. As shown in Fig. 5, CeO_2 exhibits visible light absorption with an absorption band edge at 456 nm. Pure Ag_2O shows an obvious absorption in the whole visible light region, which is in accordance with the previous reports [30]. After the attachment of Ag_2O on surface of CeO_2 , all composites show an enhanced absorption capability in visible light region. Moreover, the higher the amount of Ag_2O loaded, the stronger the visible light absorption exhibited. In general, the band edge (E_g) of the semiconductor can be estimated via the following equation: $E_g = 1240/\lambda$ [36]. Herein, λ equals the wavelength (nm) of the absorption edge. Thus, the band gap (E_g) was estimated to be about 2.72 eV for CeO_2 . Based on previous researches, the band gaps (E_g) of Ag_2O is about 1.30 eV [37].

3.2. Photocatalytic performance study

The photocatalytic performances of the as-fabricated samples were evaluated by degradation of EFA under visible light irradiation. As presented in Fig. 6a, the degradation of EFA is not observed in blank experiments in the absence of photocatalyst, indicating that the direct photolysis of EFA can be ignored. The removal of EFA for pure Ag_2O was 42.95% within 120 min, while there was almost no degradation for pure CeO_2 under the same condition. As expected, all the $\text{Ag}_2\text{O}/\text{CeO}_2$ heterojunction photocatalysts display higher photocatalytic activity than the single-component samples. The removal efficiencies of EFA are about 11.71%, 42.95%, 65.19%, 78.21%, 87.11%, 71.18% for CeO_2 , Ag_2O , AOC-1, AOC-2, AOC-3 and AOC-4, respectively. Obviously, AOC-3 exhibited the highest degradation efficiency towards EFA degradation. The loading amount of Ag_2O in $\text{Ag}_2\text{O}/\text{CeO}_2$ composites plays a

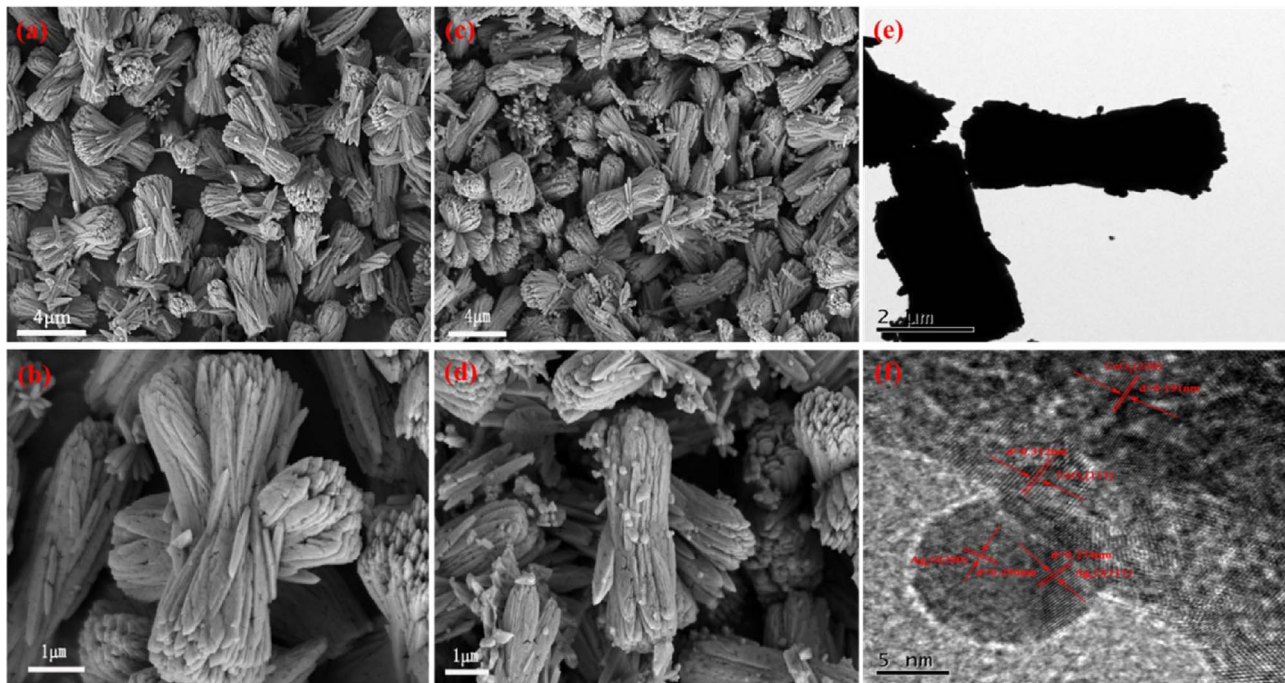


Fig. 2. (a-b) Typical SEM images of CeO₂; (c-d) AOC-3 samples; (e) TEM image of AOC-3; (f) HRTEM image of AOC-3.

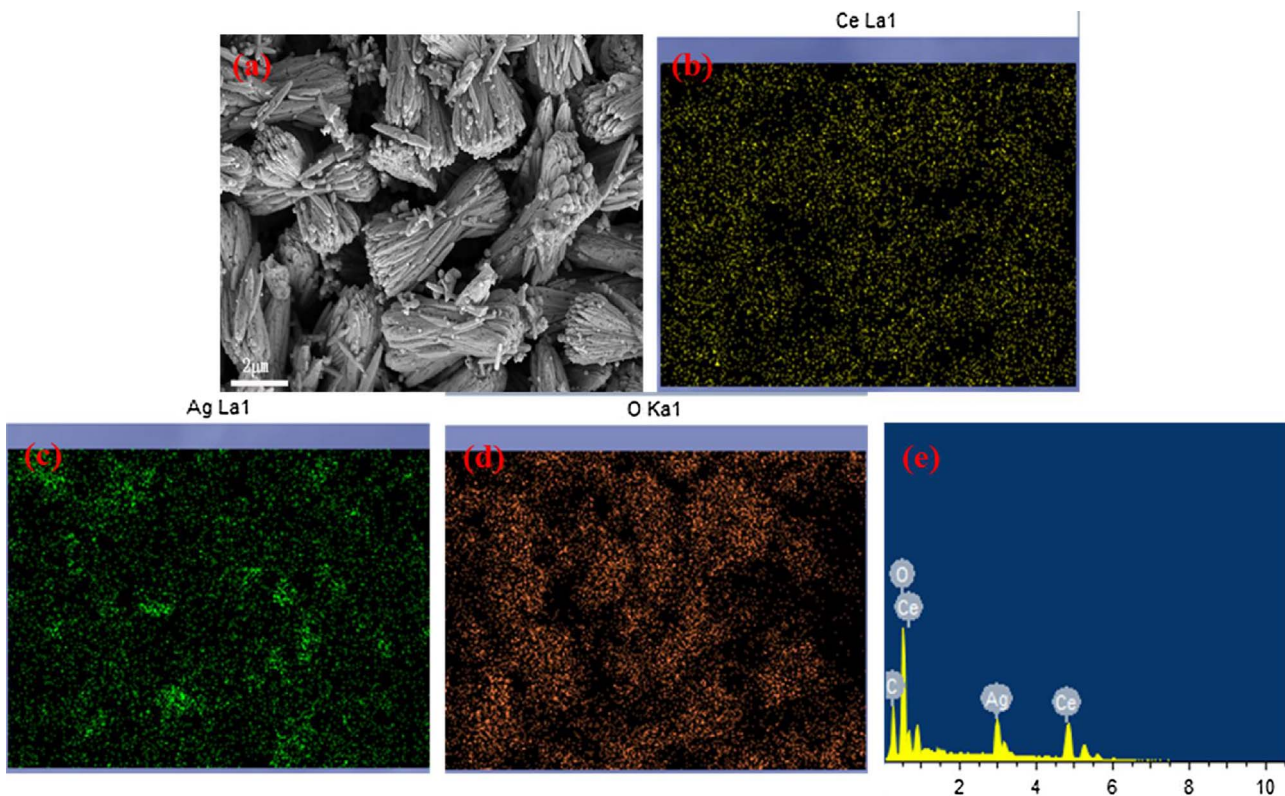
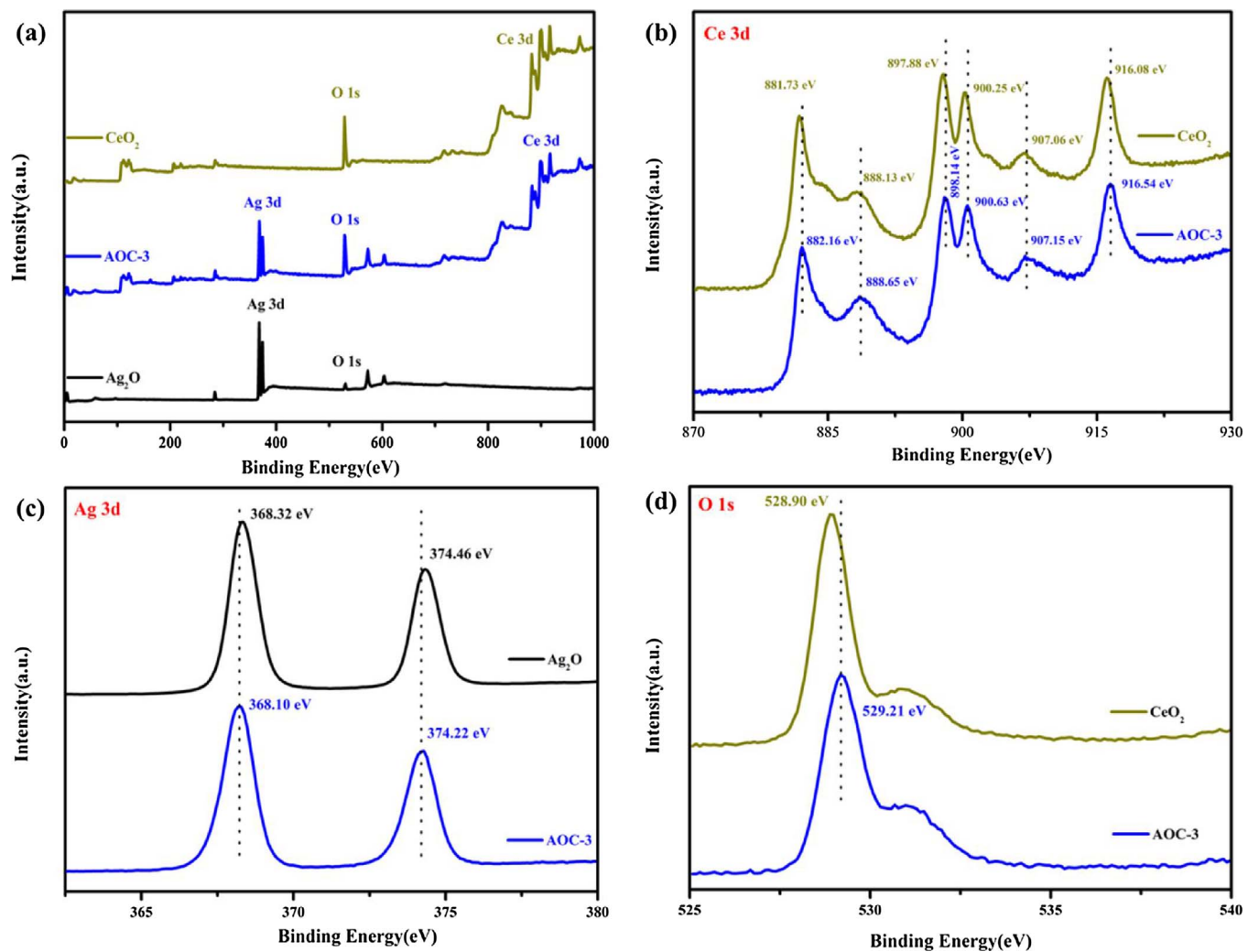
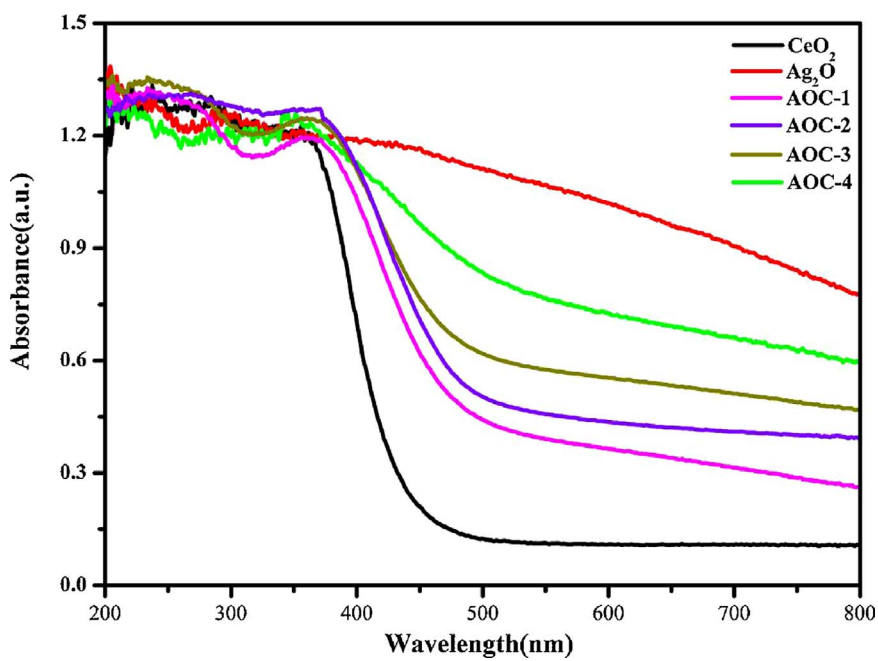


Fig. 3. SEM-EDS elemental mapping images of AOC-3 composite.

significant impact on their photocatalytic performances. Note that the photocatalytic activity enhanced when the content of Ag₂O increased from 10.29 to 25.82 wt%. This can be attributed to the fact that the increase of the amount of Ag₂O (less than 25.82 wt%) may form more active sites in this system, which would enhance the photocatalytic activity of the catalysts. When the loading amount of Ag₂O is over 25.82 wt%, a shading effect and aggregation of Ag₂O nanoparticles would gradually emerge, which could restrict the photocatalytic

performance. Fig. S1 shows the changes of the UV-spectra of EFA during the photodegradation process. The typical absorption peak of EFA gradually decreased as the irradiation time prolonging. After 120 min of visible light irradiation, it became almost disappeared, suggesting that most of the EFA can be degraded.

The photodegradation of EFA process was fitted using a following pseudo-first-order kinetic model: $\ln(C_t/C_0) = -kt$ (where C_t and C_0 are organic pollutants concentration at each given time and $t = 0$,

Fig. 4. XPS spectra of CeO_2 , Ag_2O and AOC-3 sample: (a) survey spectrum, (b) Ce 3d, (c) Ag 3d, (d) O 1s.Fig. 5. UV-vis DRS spectra of CeO_2 , Ag_2O and $\text{Ag}_2\text{O}/\text{CeO}_2$ composites.

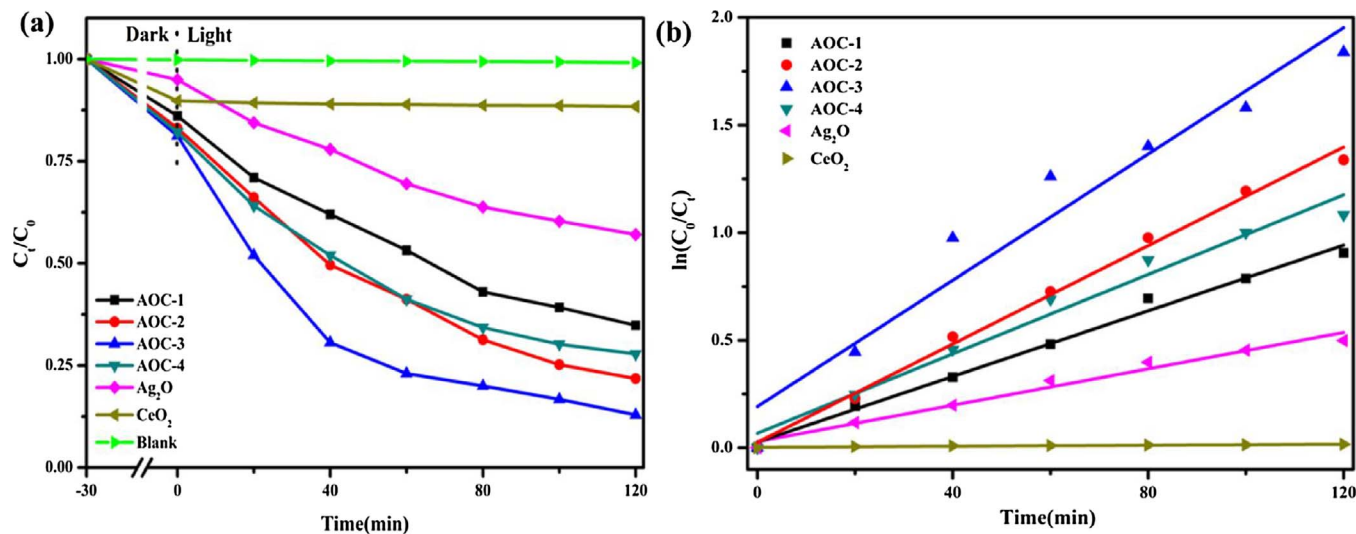


Fig. 6. (a) Photocatalytic degradation EFA curves; (b) Kinetic curves of EFA degradation.

Table 1
Pseudo-first-order rate constants (k) and correlation coefficients (R^2) for the degradation EFA in different catalysts.

Samples	$K(\text{min}^{-1})$	R^2
CeO_2	0.00012	0.9828
Ag_2O	0.00423	0.9758
AOC-1	0.00763	0.9899
AOC-2	0.01143	0.9934
AOC-3	0.01467	0.9732
AOC-4	0.00923	0.9721

respectively. And the rate constant k is the slope of the corresponding fitting curves, t represents the reaction time.)^[38] As shown in Fig. 6b, the fitting curves of EFA photocatalytic degradation are accorded with the first-order reaction dynamics. The reaction rate constant (k) of the as-obtained samples was listed in Table 1. Undoubtedly, AOC-3 displayed the highest rate constant (0.01467 min^{-1}) and that is 3.5 times higher than that of pure Ag_2O .

3.3. Possible degradation pathway of EFA

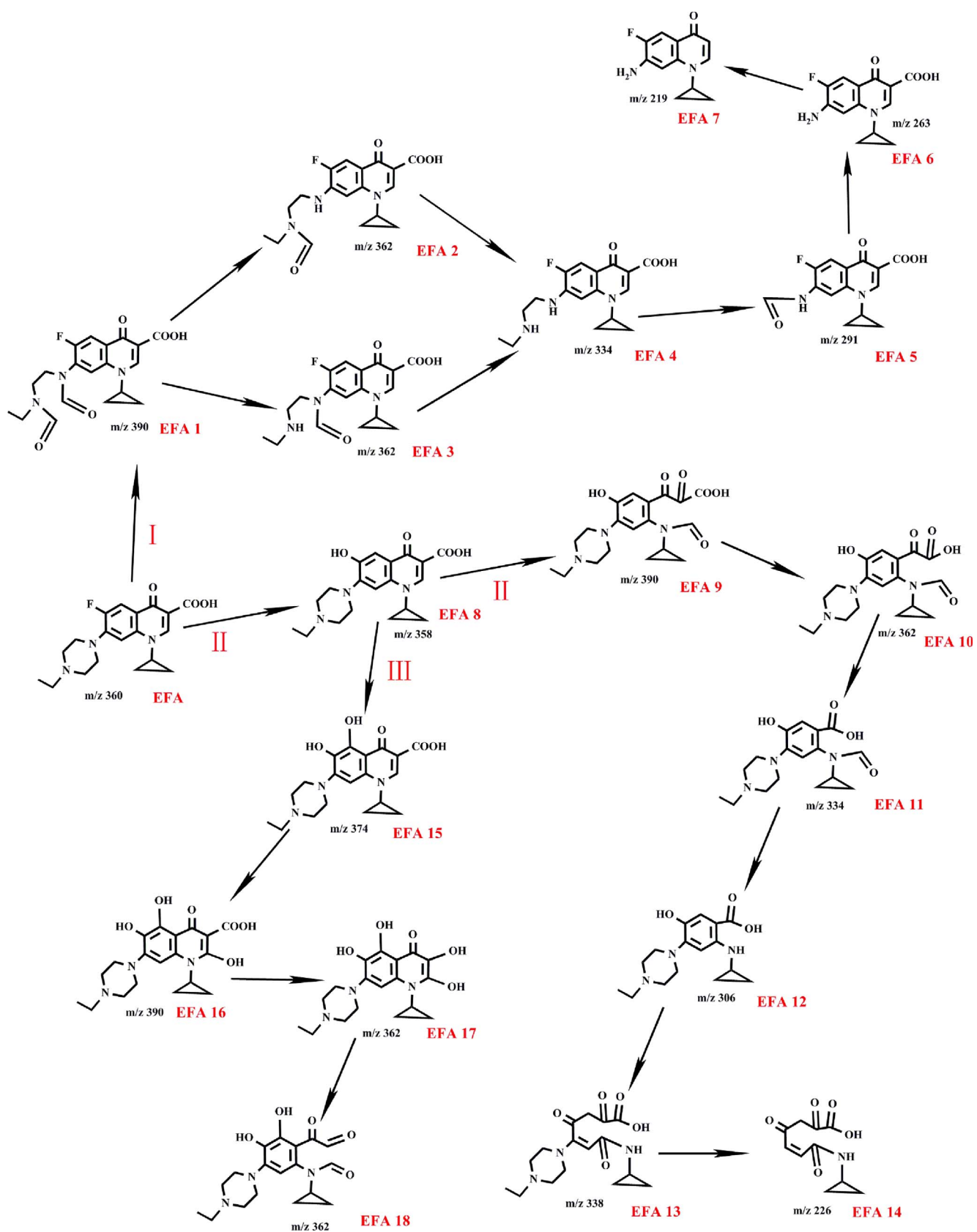
A typical chromatogram towards EFA degradation aqueous solution at 0 min and 80 min of irradiation in presence of AOC-3 was shown in Fig. S2. Obviously, only a typical ions spectra was detected at $RT = 6.44 \text{ min}$ in EFA original solution. The m/z is 360.2, which is consistent with the molecular weight of EFA with a positive ion model, indicating the typical ions spectra ascribed to the EFA molecules. After 80 min visible light irradiation, different ions spectra were detected. The different ions spectra attribute to the formation of different intermediate products. These intermediate products are identified by LC-MS technique and their information is listed in Table S1. All MS spectra of the EFA and possible intermediates were displayed in Fig. S3.

According to the identified intermediate products and the related literatures, the possible photocatalytic degradation pathways of EFA are proposed and shown in Scheme 1. Possible three main pathways were presented as follows: Pathway I is mainly the loss of piperazinyl group. Firstly, the piperazine ring was oxidized and opened to form the compound EFA 1. Subsequently, the compound EFA 1 loses two $-\text{CO}$ group and changed to the EFA 4. EFA 4 was further oxidized and produced EFA 5. EFA 5 can further transfer to EFA 6 by losing $-\text{CO}$ group. EFA 6 was further transformed EFA 7 by decarboxylation. Ultimately, the piperazinyl substituent of EFA was completely destroyed. This pathway is similar with the previous reports [39–41]. Pathway II mainly includes

the open of quinolone moieties, benzene ring and the loss of the piperazinyl substituent. Under the action of hydrolysis, the fluorine atom in EFA was substituted with a hydroxyl group and formed the compound EFA 8. Because of the strong oxidizing capacity of the reactive groups, the quinolone and benzene rings would be destroyed in succession and generated the compound EFA 9–EFA 13 in turn. EFA 13 could form simpler compound EFA 14 though removal of piperazinyl moieties. A similar pathway has been present in norfloxacin degradation by Ding et al. [42] Thus, the structure of the EFA was destroyed. Pathway III is mainly hydrolysis. The fluorine atom in EFA was firstly substituted with a hydroxyl group and formed EFA 8. EFA 8 can be further hydrolyzed and changed to EFA 15–17. This pathway has been reported in photocatalytic degradation of CIP [4]. Because of the structure of EFA 17 is instable, Then, the quinolone ring broke and formed EFA 18. Additionally, EFA 7, EFA 14 and EFA 18 can also undergo a series of reactions such as the cleavage of quinolone and/or piperazine rings, hydroxylation, decarboxylation, and are finally mineralized to CO_2 , H_2O , NO_3^- and F^- [6,43]. Herein, we cannot present this part of the degradation route. Because different radicals may be involved the degradation route and we can continue to study in later studies. This hypothesis can be concluded from the high TOC removal discussed latter.

3.4. Evaluations of mineralization activity towards EFA degradation

In addition to assess the photocatalytic degradation ability of the obtained samples, the mineralization degree of catalysts towards organic contaminants is also worth to investigate. Fig. S4 showed the change of the total organic carbon (TOC) in degradation process. For bare CeO_2 , TOC in the solution keep almost unchanged within 160 min, indicating that EFA was not degraded, which in accordance with the photodegradation results. In terms of the pure Ag_2O and the $\text{Ag}_2\text{O}/\text{CeO}_2$ composites, TOC in the solution lower in varying degrees with the prolongation of degradation time. The mineralization activity was significantly slower in comparison with degradation rate. It mainly ascribed to the generation of intermediate products. As the lighting time is extended from 120 to 160 min, TOC in the solution can continue to decrease, indicating the intermediate products can also be further mineralized. The removal rate of TOC reached up to 66.82% within the 160 min in presence of the AOC-3. Additionally, 3D EEMs could also monitor the EFA degradation and mineralization ability to a certain extent. Fluoroquinolones (FQs) can produce fluorescence due to their conjugated heterocycle structure [44]. As shown in Fig. 7a, the EFA solution mainly contain two kinds of fluorescence peaks at E_{x}



Scheme 1. Suggested photocatalytic degradation pathways of EFA.

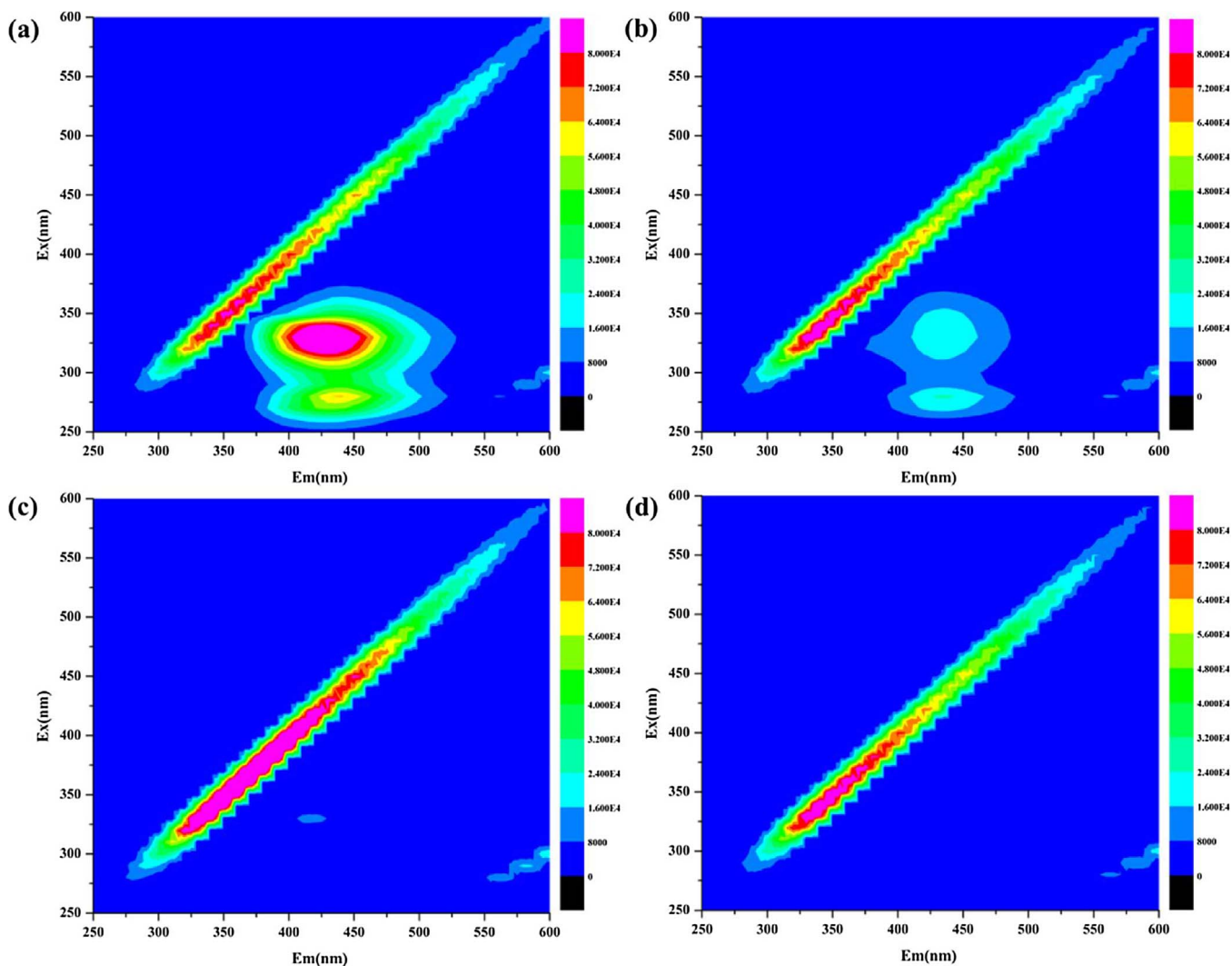


Fig. 7. Three-dimensional excitation-emission matrix fluorescence spectra (3D EEMs) of the EFA solution after visible light irradiation durations of 0 min, 40 min, 80 min and 120 min.

$E_m = 250\text{--}300/400\text{--}500\text{ nm}$ and $E_x/E_m = 300\text{--}350/400\text{--}500\text{ nm}$. According to Chen's research results [45], the EFA can be regarded as a humic acid-like substance. Under visible light irradiation, the peaks disappear gradually, indicating the concentration of EFA decreases gradually (Fig. 7b,c). The main reason may be that the conjugated heterocycle structure of EFA or intermediate products formed in degradation pathways of EFA was destroyed, which can be seen from the LC-MS analysis. When the time of the visible light irradiation reached to 120 min, the peaks cannot be observed (Fig. 7d), suggesting that EFA molecules can be degraded. Therefore, 3D EEMS results further indicate most of the EFA molecules can be removed by photocatalytic degradation.

In practice, the good repeatability and stability of photocatalysts are beneficial to reduce water treatment costs and avoid secondary pollution. We further evaluate the stability of the obtained photocatalyst by a cycling degradation experiment. AOC-3 was chose as typical catalyst and conducted on cycling experiment. From Fig. 8a, after four consecutive cycles, the photocatalytic performance of AOC-3 photocatalyst can also be maintained at a high level, indicating the good photostability of the as-prepared samples. Moreover, the XRD pattern of the used AOC-3 after four cycles of photodegradation testing was shown in Fig. 8b. As present in Fig. 8b, the peaks of the Ag appeared, signifying only partial Ag NPs generated during the photogradation process. This part of the metallic Ag can play a role of the anti-photocorrosion, thereby improving the catalyst stability. The Ag XPS spectrum of the

AOC-3 before and after four cycle's photoreaction is displayed in Fig. 8c. As revealed in Fig. 8c, a slight shift can be observed after photoreaction, which can be due to the generation of Ag. As for Fig. 8d, the peak can be further resolved into four peaks. The peaks located at 367.90 eV, 368.30 eV, 374.00 eV and 374.35 eV match with $\text{Ag}^+ 3d_{5/2}$, $\text{Ag}^0 3d_{5/2}$, $\text{Ag}^+ 3d_{3/2}$, and $\text{Ag}^0 3d_{3/2}$, respectively [46,47], demonstrating that Ag occurred during the photodegradation process. In order to further investigate the stability of the $\text{Ag}_2\text{O}/\text{CeO}_2$ composites during the photocatalytic degradation, ICP instrument was also used to detect the release of the Ag^+ in the solution after each cycle. The results were summarized in Table S2. It was found that the concentration of silver ions released in the reaction is low and the concentration of silver ions released in each cycle is almost constant. According to the reaction condition, the amount of Ag released in solution was calculated to about 2.0 μg , which is only a fraction of the total Ag. Thus, it can be inferred that catalyst has good stability during the photocatalytic reaction. Based on the above demonstrations, it can be deduced that the $\text{Ag}_2\text{O}/\text{CeO}_2$ composites possess excellent photocatalytic performance, as well as good stability.

3.5. Photocatalytic mechanism study

The main active species formed in the photocatalytic degradation process were determined for investigating photocatalytic mechanism. Scavengers ($\text{Na}_2\text{C}_2\text{O}_4$, BQ and IPA) were separately added to capture

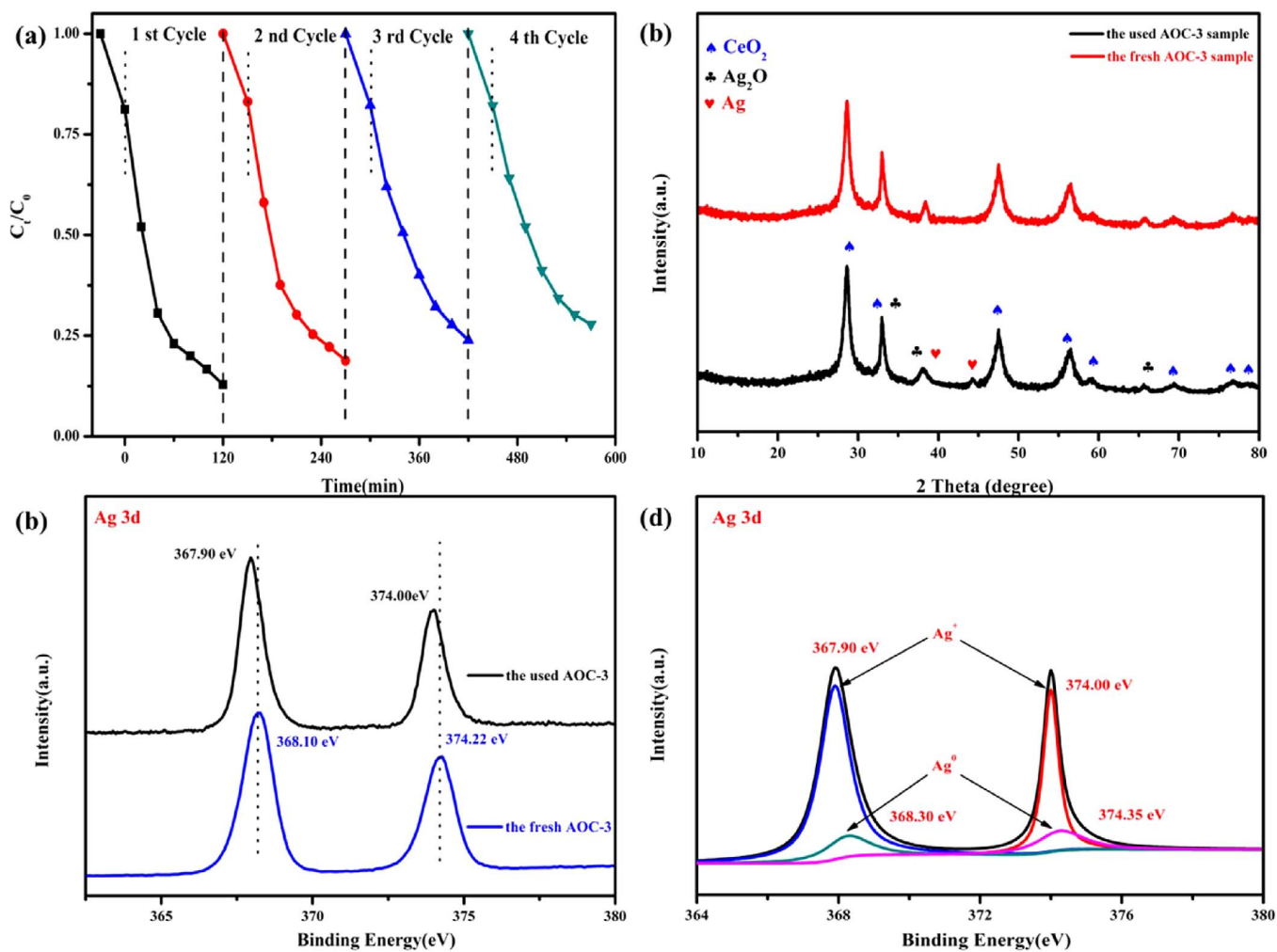


Fig. 8. (a) Cycling photocatalytic test of AOC-3; (b) XRD patterns of AOC-3 before and after photocatalytic tests; (c) Ag XPS spectrum of the AOC-3 before and after photoreaction; (d) Ag XPS spectrum of the AOC-3 after photoreaction.

holes, $\cdot\text{O}_2^-$ and $\cdot\text{OH}$ [48,49]. As presented in Fig. 9a, the degradation efficiency was significantly reduced from 87.11% to 48.19% and 64.24% in the presence of BQ and $\text{Na}_2\text{C}_2\text{O}_4$, indicating that $\cdot\text{O}_2^-$ and h^+ play a dominant role in decomposition process of EFA. Note that there is slightly decrease in the degradation rate of EFA with the introduction of IPA, suggesting that $\cdot\text{OH}$ is not a major active species in the degradation process. Moreover, after bubbling nitrogen to remove oxygen in solution, the degradation efficiency dramatically decreases to 41.23%, illuminating that the oxygen dissolved in solution plays an important role in the generation of active species.

Electron spin resonance (ESR) instrument was implemented to detect the generation of $\cdot\text{O}_2^-$ and $\cdot\text{OH}$ in the presence of AOC-3 composites. As displayed in Fig. 9c, when the samples exposed to visible light, six typical signals were detected in methanol solution, while no signal could be observed in dark, indicating that $\cdot\text{O}_2^-$ was formed in this process. Meantime, no obvious signals were collected in aqueous even after lighting on 12 min (Fig. 9d), verifying $\cdot\text{OH}$ radicals is not main active species in the photocatalysis process.

Generally, photoluminescence spectra (PL) can reflect the transfer efficiency of the charge carriers. Commonly, the low photocatalytic performance corresponds to the high fluorescence intensity [50]. Fig. 10 displays the PL spectra of the pure CeO_2 and all the composites with an excitation wavelength of 325 nm. It can be seen that all samples exhibit similar shapes. However, the composites show significantly diminished PL intensity in comparison to pristine CeO_2 sample, demonstrating that coupling with Ag_2O is favorable for the separation of

charge carriers. It should be noted that AOC-3 displays the lowest PL intensity in all composites, implying the highest recombination rate of photoexcited electron–hole pairs.

On the other hand, the photocurrent density can also be a valid technique to reveal the transfer property of the photogenerated electrons, meanwhile the higher photocurrent density represents higher segregation efficiency of the photogenerated carriers [51]. The transient photocurrent intensity of the pure CeO_2 and $\text{Ag}_2\text{O}/\text{CeO}_2$ composites were tested in light on/off cycles, and the results are exhibited in Fig. 11a. As shown in Fig. 11a, all samples produce photocurrent under visible light irradiation, indicating that they can be responded under visible light irradiation and generated electrons and holes. Comparatively, AOC-3 displays the highest photocurrent intensity, confirming the best separation efficiency of photogenerated electron–hole pairs. Further, the electrochemical impedance spectroscopy (EIS) is implemented to further quest the charge transport capability of the samples under visible light irradiation. As is well-known, the smaller arc radius indicates a less obstruction for the transfer of electrons–holes, meaning more efficient separation efficiency of the charge [52]. As displayed in Fig. 11b, the radius of the sample is arranged as follows: $\text{CeO}_2 > \text{AOC-1} > \text{AOC-4} > \text{AOC-2} > \text{AOC-3}$. Distinctly, AOC-3 is the smallest arc radius, meaning the least resistance for charge transfer, which is corresponding with the results of the photocurrent.

The Mott-Schottky tests were applied to confirm flat band potential and semiconductors types of the pure CeO_2 and Ag_2O . The flat band potential of the semiconductors can be ascertained using the following

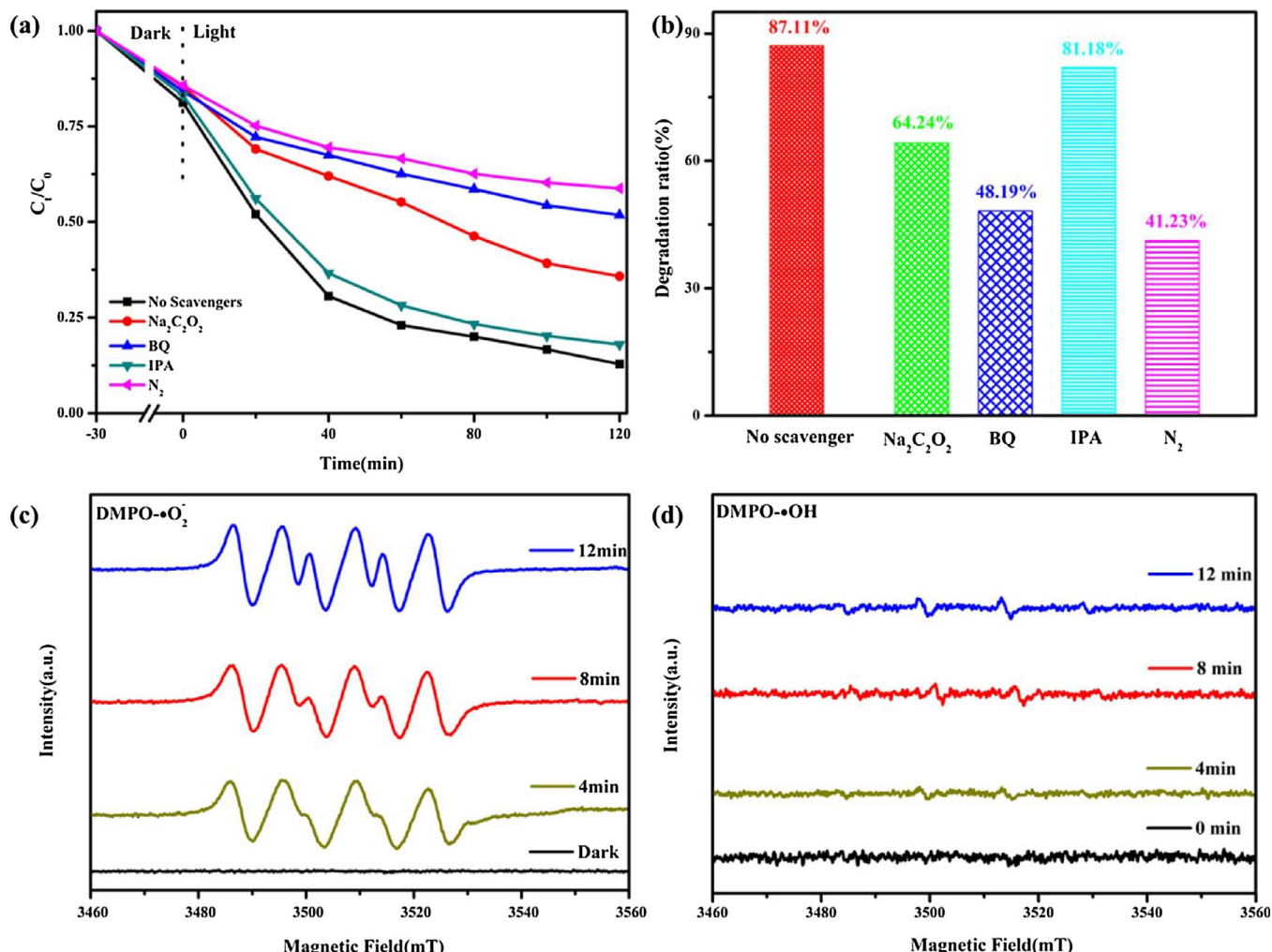


Fig. 9. (a) Photocatalytic curves of AOC-3 composites with different scavengers for the degradation of EFA; (b) The degradation values towards EFA degradation after introduction of difference scavengers; (c) DMPO spin-trapping ESR spectra for AOC-3 in methanol dispersion for DMPO-•O₂⁻ and (d) aqueous dispersion for DMPO-•OH.

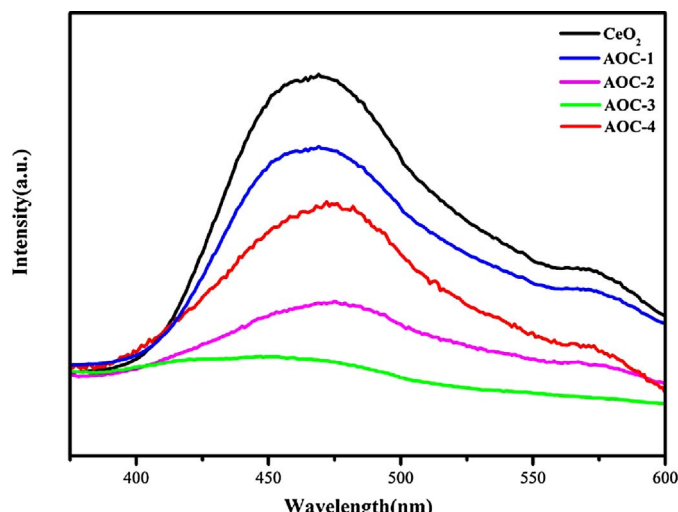


Fig. 10. PL spectra of CeO₂ and Ag₂O/CeO₂ composites.

equation [53]:

$$\frac{1}{c^2} = \frac{2}{q\epsilon\epsilon_0 N_d} \left(E - E_{fb} - \frac{K_b T}{q} \right)$$

In this equation, ϵ and ϵ_0 are the dielectric constants of the

semiconductor and permittivity of free space, C , N_d , E , K_b , T , and q represent the space charge capacitance, donor density, applied potential, Boltzmann's constant, temperature, and electronic charge, respectively. The E_{fb} of CeO₂ is calculated to be -0.450 V versus an Ag/AgCl electrode (SCE), which is -0.253 eV versus a normal hydrogen electrode (NHE). Additionally, CeO₂ can be regarded as *n*-type semiconductors due to the positive slope of Mott–Schottky curve (Fig. 12a). Similarly, The E_{fb} of Ag₂O is calculated to be 0.957 eV (NHE) and Ag₂O revealed the negative slope of Mott–Schottky curve (Fig. 12b), indicating it is *p*-type semiconductors [54]. An inverted “V-shape” Mott–Schottky curve can be observed in Fig. 12c, indicated *n*-*p* junction exists in Ag₂O/CeO₂ composites [55].

Combined with the results of various characterization analysis and photocatalytic degradation experiments, the mechanism of enhanced photocatalytic performance over Ag₂O/CeO₂ under visible light irradiation was elucidated and shown in Scheme 2. Based on the results of Mott–Schottky curves, the band positions of Ag₂O and CeO₂ before contact are displayed in Scheme 2a. The Fermi level of Ag₂O approaches to the (valence band) VB. Inversely, the Fermi level of CeO₂ is close to the (conduction band) CB. After the Ag₂O contacts with CeO₂ tightly, the *p*–*n* heterojunction can be formed as displayed in Scheme 2b. Then the Fermi level achieves equilibrium. Meantime, an inner electric field will be built in the interface. Under the irradiation of visible light, Ag₂O can be excited and generate electrons and holes. Since the CB potential of the Ag₂O is more negative than that of the CeO₂, the electrons on the CB of the Ag₂O can transfer to that of CeO₂.

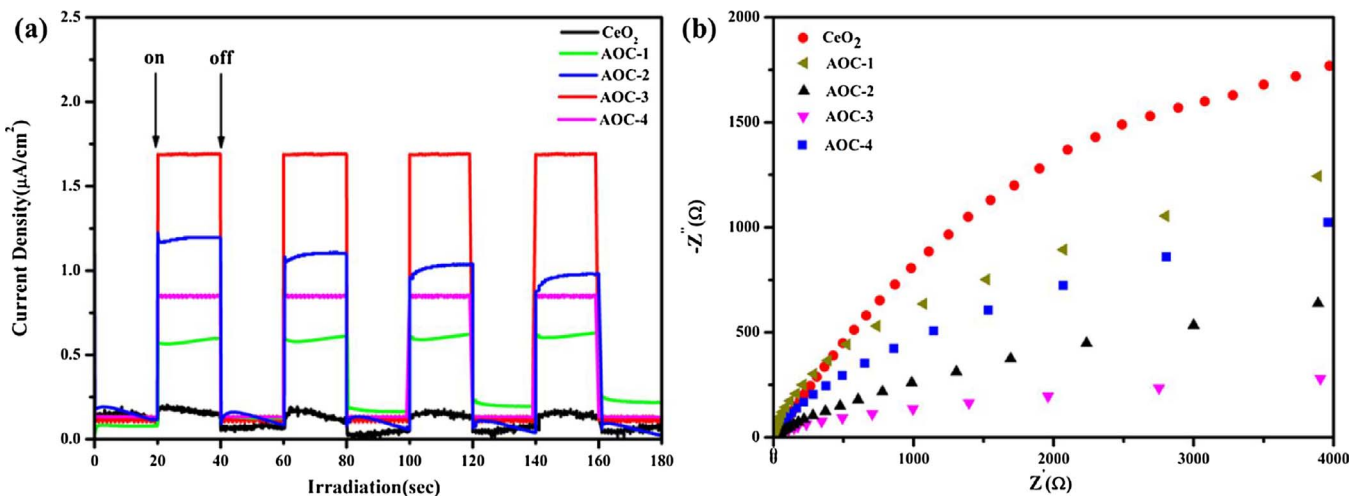


Fig. 11. (a) Transient photocurrent response for the pure CeO_2 and $\text{Ag}_2\text{O}/\text{CeO}_2$ heterojunction under visible light irradiation; (b) EIS Nyquist plots of the pure CeO_2 and $\text{Ag}_2\text{O}/\text{CeO}_2$ hybrids.

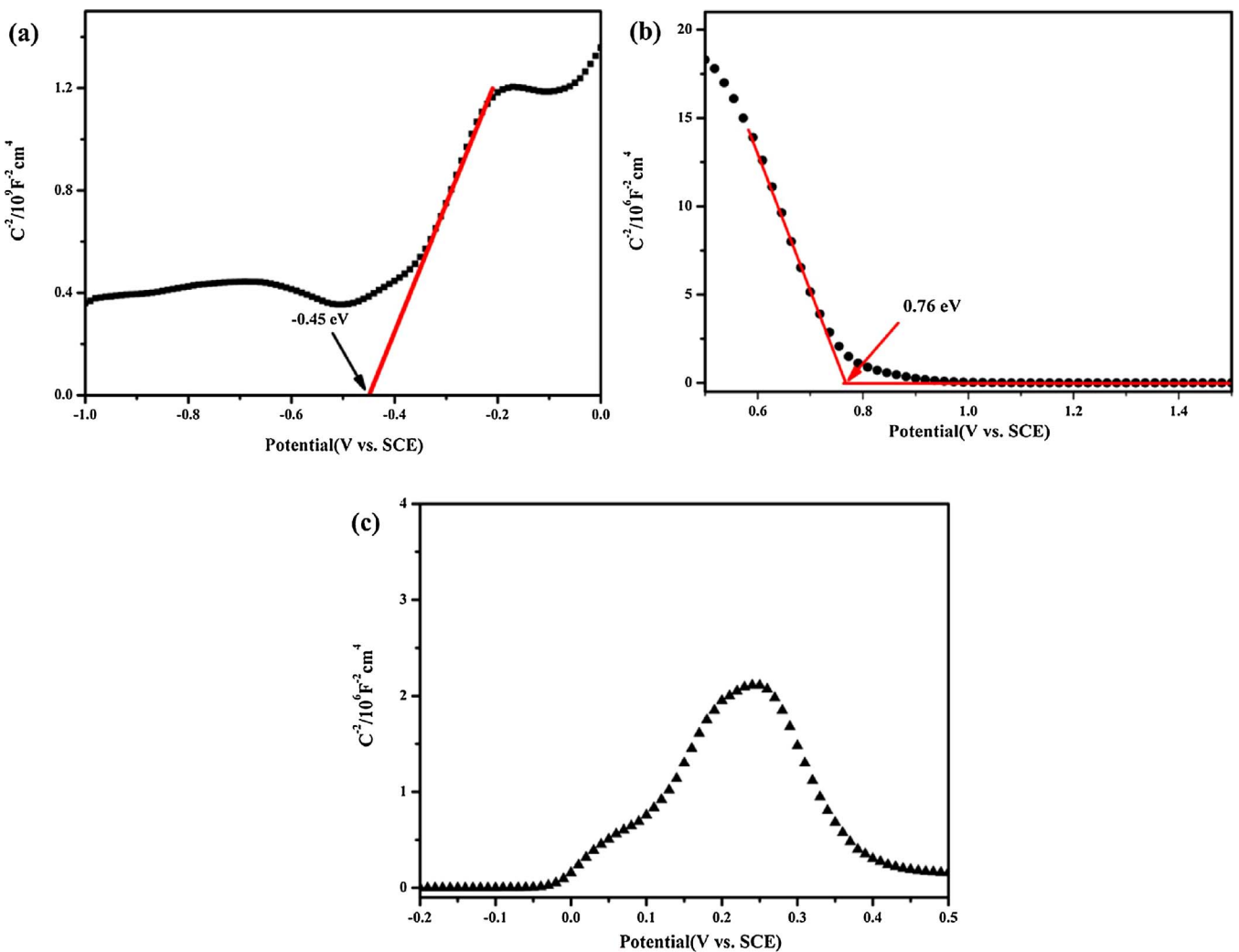
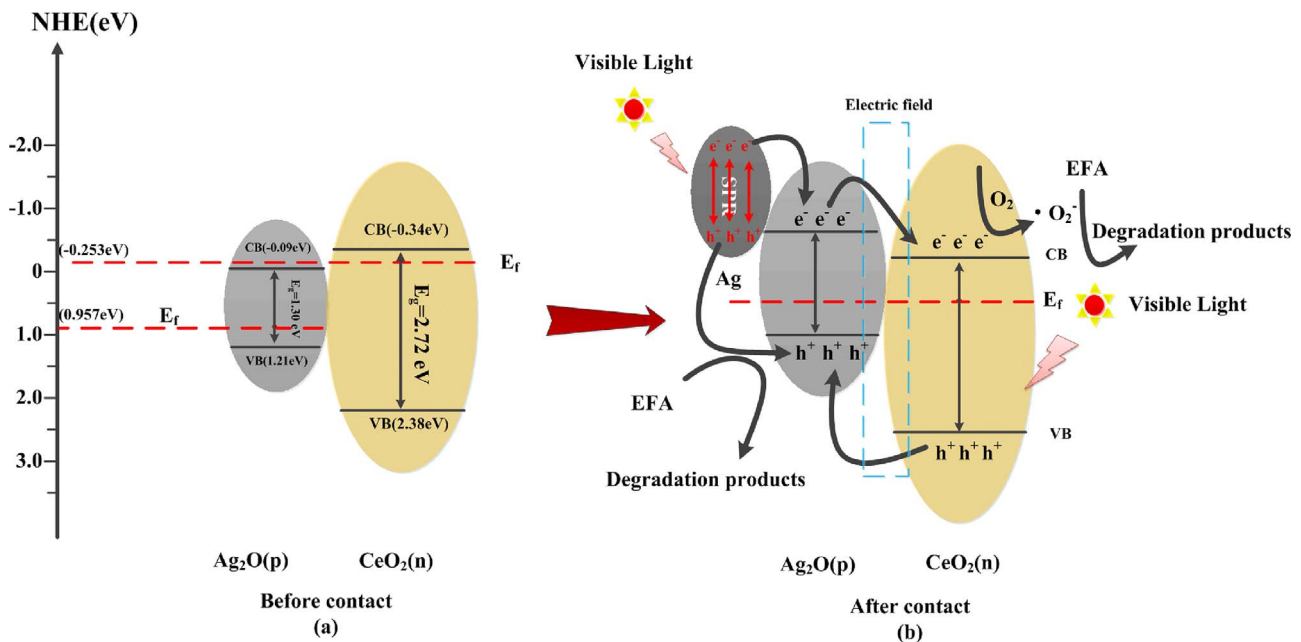


Fig. 12. Mott–Schottky curves of CeO_2 , Ag_2O and AOC-3.

On the other side, Ag NPs can be excited to form electrons and holes through SPR effect. The energy of excited hot electrons was between 1.0 and 4.0 eV [56,57], so that the electrons could migrate to the CB of Ag_2O . Ultimately, the electrons generated in $\text{Ag}_2\text{O}/\text{CeO}_2$ hybrids were gathered onto the CB of the CeO_2 , which could further react with O_2 in

the solution to produce $\cdot\text{O}_2^-$. The $\cdot\text{O}_2^-$ could effectively degrade organic pollutants. In addition, a part of the holes formed in $\text{Ag}_2\text{O}/\text{CeO}_2$ composites would move to the surface of Ag_2O , which can directly degrade the EFA. Simultaneously, the stability of the $\text{Ag}_2\text{O}/\text{CeO}_2$ heterojunction photocatalyst could also be greatly improved due to the



Scheme 2. The proposed mechanism for the enhancement of photocatalytic activity.

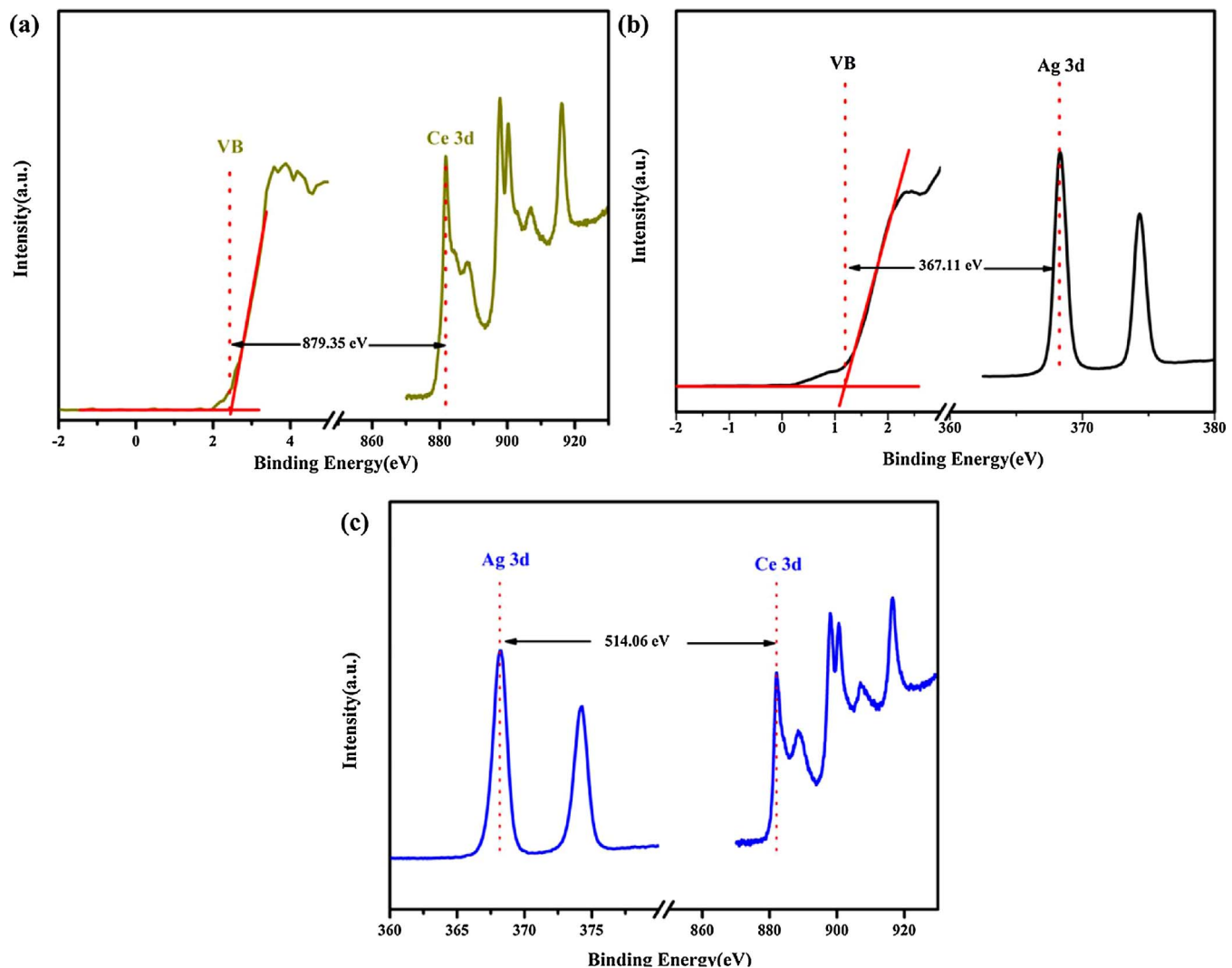
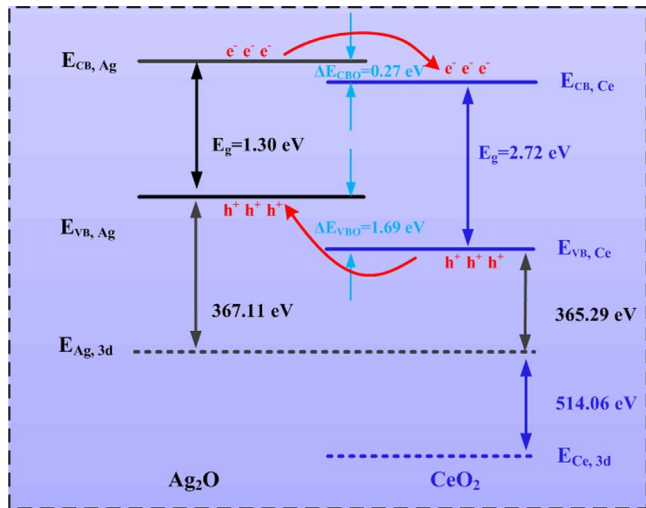
Fig. 13. XPS core-level and valence band spectra obtained from (a) CeO₂, (b) Ag₂O, (c) AOC-3.

Table 2

XPS Binding Energies of the Core Levels, VBM and the Band-Gap Energy for Ag_2O , CeO_2 , and $\text{Ag}_2\text{O}/\text{CeO}_2$ Photocatalysts.

samples	state	Binding energy (eV)	E_g (eV)
CeO_2	$\text{Ce } 3\text{d}_{5/2}$	881.73	2.72
	VBM	2.38	
Ag_2O	$\text{Ag } 3\text{d } 7/2$	368.32	1.30
	VBM	1.21	
$\text{Ag}_2\text{O}/\text{CeO}_2$	$\text{Ag } 3\text{d}_{5/2}$	368.10	1.30
	$\text{Ce } 3\text{d}$	882.16	

**Scheme 3.** Energy band diagrams of $\text{Ag}_2\text{O}/\text{CeO}_2$ heterojunctions.

efficiently transfer of electrons from Ag_2O . In sum, by building a *p-n* heterojunction in $\text{Ag}_2\text{O}/\text{CeO}_2$ composites, not only can greatly enhance the visible light photocatalytic activity of $\text{Ag}_2\text{O}/\text{CeO}_2$ hybrids, but also improve its stability remarkably.

The band alignment of the $\text{Ag}_2\text{O}/\text{CeO}_2$ composites is calculated for further proving the above proposed mechanism. The band offset of $\text{Ag}_2\text{O}/\text{CeO}_2$ heterojunction can be estimated by the method of Kraut [58]. The core level positions and the valence band maximum (VBM) positions of Ag_2O and CeO_2 were confirmed by XPS technique. The valence-band offset (ΔE_{VBO}) and conduction-band offset (ΔE_{CBO}) of the $\text{Ag}_2\text{O}/\text{CeO}_2$ heterostructure were calculated using the following equation [59]:

$$\Delta E_{VBO} = (E_{Ce,3d} - E_{VB,Ce})_{pure}^{CeO_2} - (E_{Ag,3d} - E_{VB,Ag})_{pure}^{Ag_2O} + \Delta E_{CL}$$

$$\Delta E_{CBO} = E_g^{CeO_2} - E_g^{Ag_2O} + \Delta E_{VBO}$$

Herein, $\Delta E_{CL} = (E_{Ag,3d} - E_{Ce,3d})$ is the energy difference between Ag 3d and Ce 3d core levels in the $\text{Ag}_2\text{O}/\text{CeO}_2$ heterostructure. $E_{Ag,3d}$ and $E_{Ce,3d}$ are the core level binding energies of Ag and Ce elements in the pure Ag_2O and CeO_2 , respectively; $E_{V,Ce}$ and $E_{V,Ag}$ are the VB of the CeO_2 and Ag_2O , respectively. $E_g^{Ag_2O}$ and $E_g^{CeO_2}$ are the band gap of Ag_2O and CeO_2 , respectively.

As shown in Fig. 13, the VBM value for the Ag_2O and CeO_2 sample was calculated to be 1.21 eV and 2.38 eV, respectively. The value between the core-level positions and VBM for CeO_2 and Ag_2O is 879.35 and 367.11 eV. The difference between Ce 3d and Ag 3d core levels in the $\text{Ag}_2\text{O}/\text{CeO}_2$ heterostructure is 514.06 eV. The binding energy values for the core-level, VBM, and band-gap energy of Ag_2O , CeO_2 and $\text{Ag}_2\text{O}/\text{CeO}_2$ heterojunctions were summarized in Table 2. Base on the above equations, the ΔE_{VBO} and ΔE_{CBO} values for $\text{Ag}_2\text{O}/\text{CeO}_2$ heterojunctions could be calculated to be -1.69 eV and -0.27 eV, respectively. The negative value indicates that the CB and VB of CeO_2 are lower than that of Ag_2O . The energy band alignment of the $\text{Ag}_2\text{O}/\text{CeO}_2$ heterojunction

photocatalyst is proposed in Scheme 3. The ΔE_{CBO} is the driving force that can promote the photogenerated electrons to transfer from the Ag_2O to the CeO_2 ; and ΔE_{VBO} is the driving force that can promote the photogenerated holes to transfer from the CeO_2 to the Ag_2O [60]. The results of the band alignment can further confirm a *p-n* junction formed between CeO_2 and Ag_2O .

4. Conclusion

To sum up, a novel $\text{Ag}_2\text{O}/\text{CeO}_2$ *p-n* junction photocatalysts were triumphantly fabricated via an *in situ* loading Ag_2CO_3 on CeO_2 spindles and subsequent via a thermal decomposition process. The $\text{Ag}_2\text{O}/\text{CeO}_2$ composites exhibited outstanding photocatalytic activity for the photodegradation of EFA under visible light irradiation. Three possible degradation pathways of EFA were proposed based on LC-MS analysis. The investigation of the 3D EEMs and TOC indicates high mineralization ability towards the EFA molecule degradation in presence of $\text{Ag}_2\text{O}/\text{CeO}_2$ composites. Transient photocurrent response, PL spectrum and EIS indicate higher photoinduced charge separation efficiency possess in $\text{Ag}_2\text{O}/\text{CeO}_2$ composites. Active species trapping experiments and ESR technique confirmed that h^+ and $\cdot\text{O}_2^-$ were the main active groups involved in photo-degradation of organic pollutants. It is expected that the $\text{Ag}_2\text{O}/\text{CeO}_2$ composites could be used as a promising photocatalyst for energy conversion and environmental remediation. This work could provide a new approach to construct new *p-n* junction photocatalysts and a deeper insight for the heterojunction catalyst.

Acknowledgements

This work was supported by the National Natural Science Foundation of China (NSFC) (51541801, 51521006).

Appendix A. Supplementary data

Supplementary data associated with this article can be found, in the online version, at <http://dx.doi.org/10.1016/j.apcatb.2017.09.060>.

References

- [1] A. Jia, Y. Wan, Y. Xiao, J.Y. Hu, Occurrence and fate of quinolone and fluorquinolone antibiotics in a municipal sewage treatment plant, *Water Res.* 46 (2012) 387–394.
- [2] T.S. Anirudhan, F. Shainy, J. Christa, Synthesis and characterization of polyacrylic acid grafted-carboxylic graphene/titanium nanotube composite for the effective removal of enrofloxacin from aqueous solutions: adsorption and photocatalytic degradation studies, *J. Hazard. Mater.* 324 (2017) 117–130.
- [3] W. Yan, J.F. Zhang, C.Y. Jing, Enrofloxacin transformation on *shewanella oneidensis* MR-1 reduced goethite during anaerobic-Aerobic transition, *Environ. Sci. Technol.* 50 (2016) 11034–11040.
- [4] C.L. Jiang, Y.F. Ji, Y.Y. Shi, J.F. Chen, T.M. Cai, Sulfate radical-based oxidation of fluoroquinolone antibiotics: kinetics, mechanisms and effects of natural water matrices, *Water Res.* 106 (2016) 507–517.
- [5] E. Guinea, J.A. Garrido, R.M. Rodriguez, P.L. Cabot, C. Arias, F. Centellas, E. Brillas, Degradation of the fluoroquinolone enrofloxacin by electrochemical advanced oxidation processes based on hydrogen peroxide electrogeneration, *Electrochim. Acta* 55 (2010) 2101–2115.
- [6] C. Wang, L.F. Yin, Z.S. Xu, J.F. Niu, L.A. Hou, Electrochemical degradation of enrofloxacin by lead dioxide anode: kinetics, mechanism and toxicity evaluation, *Chem. Eng. J.* 326 (2017) 911–920.
- [7] A. Zada, Y. Qu, S. Ali, N. Sun, H. Lu, R. Yan, X. Zhang, L. Jing, Improved visible-light activities for degrading pollutants on $\text{TiO}_2/\text{g-C}_3\text{N}_4$ nanocomposites by decorating SPR Au nanoparticles and 2,4-dichlorophenol decomposition path, *J. Hazard. Mater.* 342 (2018) 715–723.
- [8] Z.Y. Lu, F. Chen, M. He, M.S. Song, Z.F. Ma, W.D. Shi, Y.S. Yan, J.Z. Lan, F. Li, P. Xiao, Microwave synthesis of a novel magnetic imprinted TiO_2 photocatalyst with excellent transparency for selective photodegradation of enrofloxacin hydrochloride residues solution, *Chem. Eng. J.* 249 (2014) 15–26.
- [9] Y.Q. Yu, L. Yan, J.M. Cheng, C.Y. Jing, Mechanistic insights into TiO_2 thickness in $\text{Fe}_3\text{O}_4/\text{TiO}_2/\text{GO}$ composites for enrofloxacin photodegradation, *Chem. Eng. J.* 325 (2017) 647–654.
- [10] H. Dong, G. Zeng, L. Tang, C. Fan, C. Zhang, X. He, Y. He, An overview on limitations of TiO_2 -based particles for photocatalytic degradation of organic pollutants and the corresponding countermeasures, *Water Res.* 79 (2015) 128–146.
- [11] S. Yan, Z. Li, Z. Zou, Photodegradation performance of $\text{g-C}_3\text{N}_4$ fabricated by directly

heating melamine, *Langmuir* 25 (2009) 10397–10401.

[12] A. Kudo, K. Omori, H. Kato, A novel aqueous process for preparation of crystal form-controlled and highly crystalline BiVO_4 powder from layered vanadates at room temperature and its photocatalytic and photophysical properties, *J. Am. Chem. Soc.* 121 (1999) 11459–11467.

[13] Y. Bi, S. Ouyang, N. Umezawa, J. Cao, J. Ye, Facet effect of single-crystalline Ag_3PO_4 sub-microcrystals on photocatalytic properties, *J. Am. Chem. Soc.* 133 (2011) 6490–6492.

[14] K. Zhou, Z. Yang, S. Yang, Highly reducible CeO_2 nanotubes, *Chem. Mater.* 19 (2007) 1215–1217.

[15] P. Wang, B. Huang, X. Zhang, X. Qin, H. Jin, Y. Dai, Z. Wang, J. Wei, J. Zhan, S. Wang, Highly efficient visible-light plasmonic photocatalyst $\text{Ag}@\text{AgBr}$, *Chem. A Eur. J.* 15 (2009) 1821–1824.

[16] X.J. Wen, C.G. Niu, M. Ruan, L. Zhang, G.M. Zeng, AgI nanoparticles-decorated CeO_2 microsheets photocatalyst for the degradation of organic dye and tetracycline under visible-light irradiation, *J. Colloid Interface Sci.* 497 (2017) 368–377.

[17] F. Dvorak, O. Stetovych, M. Steger, E. Cherradi, I. Matolínová, N. Tsud, M. Skoda, T. Skála, J. Mysliveček, V. Matolín, Adjusting morphology and surface reduction of CeO_2 (111) thin films on Cu (111), *J. Phys. Chem. C* 115 (2011) 7496–7503.

[18] Y. Huang, B. Long, M. Tang, Z. Rui, M.S. Balogun, Y. Tong, H. Ji, Bifunctional catalytic material: an ultrastable and high-performance surface defect CeO_2 nanosheets for formaldehyde thermal oxidation and photocatalytic oxidation, *Appl. Catal. B* 181 (2016) 779–787.

[19] Y. Ji, C. Ferronato, A. Salvador, X. Yang, J.M. Chovelon, Degradation of ciprofloxacin and sulfamethoxazole by ferrous-activated persulfate: implications for remediation of groundwater contaminated by antibiotics, *Sci. Total Environ.* 472 (2014) 800–808.

[20] B. Xu, Q. Zhang, S. Yuan, M. Zhang, T. Ohno, Morphology control and photocatalytic characterization of yttrium-doped hedgehog-like CeO_2 , *Appl. Catal. B* 164 (2015) 120–127.

[21] N. Wetchakun, S. Chaiwichean, B. Inceesungvorn, K. Pingmuang, S. Phanichphant, A.I. Minett, J. Chen, $\text{BiVO}_4/\text{CeO}_2$ nanocomposites with high visible-light-induced photocatalytic activity, *ACS Appl. Mater. Interfaces* 4 (2012) 3718–3723.

[22] N. Tian, H. Huang, C. Liu, F. Dong, T. Zhang, X. Du, S. Yu, Y. Zhang, In situ copyrolysis fabrication of $\text{CeO}_2/\text{g}_{\text{C}_3\text{N}_4}$ n–n type heterojunction for synchronously promoting photo-induced oxidation and reduction properties, *J. Mater. Chem. A* 3 (2015) 17120–17129.

[23] S. Hu, F. Zhou, L. Wang, J. Zhang, Preparation of $\text{Cu}_2\text{O}/\text{CeO}_2$ heterojunction photocatalyst for the degradation of Acid Orange 7 under visible light irradiation, *Catal. Commun.* 12 (2011) 794–797.

[24] X.J. Wen, C. Zhang, C.-G. Niu, L. Zhang, G.M. Zeng, X.G. Zhang, Highly enhanced visible light photocatalytic activity of CeO_2 through fabricating a novel p–n junction $\text{BiOBr}/\text{CeO}_2$, *Catal. Commun.* 90 (2017) 51–55.

[25] X.J. Wen, C.G. Niu, L. Zhang, G.M. Zeng, Novel p–n heterojunction BiOI/CeO_2 photocatalyst for wider spectrum visible-light photocatalytic degradation of refractory pollutants, *Dalton Trans.* 46 (2017) 4982–4993.

[26] X. Wang, S. Li, H. Yu, J. Yu, S. Liu, Ag_2O as a new visible-light photocatalyst: self-stability and high photocatalytic activity, *Chem. Eur. J.* 17 (2011) 7777–7780.

[27] D. Sarkar, C.K. Ghosh, S. Mukherjee, K.K. Chattopadhyay, Three dimensional $\text{Ag}_2\text{O}/\text{TiO}_2$ type-II (p–n) nanoheterojunctions for superior photocatalytic activity, (2012), *ACS Appl. Mater. Interfaces* 5 (2013) 331–337.

[28] J. Zhang, H. Liu, Z. Ma, Flower-like $\text{Ag}_2\text{O}/\text{Bi}_2\text{MoO}_6$ p–n heterojunction with enhanced photocatalytic activity under visible light irradiation, *J. Mol. Catal. A: Chem.* 424 (2016) 37–44.

[29] N. Liang, M. Wang, L. Jin, S. Huang, W. Chen, M. Xu, Q. He, J. Zai, N. Fang, X. Qian, Highly efficient $\text{Ag}_2\text{O}/\text{Bi}_2\text{O}_3\text{CO}_3$ pn heterojunction photocatalysts with improved visible-light responsive activity, *ACS Appl. Mater. Interfaces* 6 (2014) 11698–11705.

[30] S. Li, S. Hu, W. Jiang, Y. Liu, J. Liu, Z. Wang, Synthesis of n-type TaON microspheres decorated by p-type Ag_2O with enhanced visible light photocatalytic activity, *Mol. Catal.* 435 (2017) 135–143.

[31] F. Chen, Q. Yang, F. Yao, S. Wang, J. Sun, H. An, K. Yi, Y. Wang, Y. Zhou, L. Wang, X. Li, D. Wang, G. Zeng, Visible-light photocatalytic degradation of multiple antibiotics by AgI nanoparticle-sensitized $\text{Bi}_2\text{O}_3\text{I}$ microspheres: enhanced interfacial charge transfer based on Z-scheme heterojunctions, *J. Catal.* 352 (2017) 160–170.

[32] P. Ji, J. Zhang, F. Chen, M. Anpo, Study of adsorption and degradation of acid orange 7 on the surface of CeO_2 under visible light irradiation, *Appl. Catal. B* 85 (2009) 148–154.

[33] O.A. Zelekew, D.-H. Kuo, J.M. Yassin, K.E. Ahmed, H. Abdullah, Synthesis of efficient silica supported $\text{TiO}_2/\text{Ag}_2\text{O}$ heterostructured catalyst with enhanced photocatalytic performance, *Appl. Surf. Sci.* 410 (2017) 454–463.

[34] L. Xu, J. Wang, Magnetic nanoscaled $\text{Fe}_3\text{O}_4/\text{CeO}_2$ composite as an efficient Fenton-like heterogeneous catalyst for degradation of 4-chlorophenol, *Environ. Sci. Technol.* 46 (2012) 10145–10153.

[35] Y. Guo, J. Li, Z. Gao, X. Zhu, Y. Liu, Z. Wei, W. Zhao, C. Sun, A simple and effective method for fabricating novel p–n heterojunction photocatalyst $\text{g}_{\text{C}_3\text{N}_4}/\text{Bi}_4\text{Ti}_3\text{O}_{12}$ and its photocatalytic performances, *Appl. Catal. B* 192 (2016) 57–71.

[36] W. Wang, L. Jing, Y. Qu, Y. Luan, H. Fu, Y. Xiao, Facile fabrication of efficient $\text{AgBr}-\text{TiO}_2$ nanoheterostructured photocatalyst for degrading pollutants and its photogenerated charge transfer mechanism, *J. Hazard. Mater.* 243 (2012) 169–178.

[37] C. Yu, G. Li, S. Kumar, K. Yang, R. Jin, Phase transformation synthesis of novel $\text{Ag}_2\text{O}/\text{Ag}_2\text{CO}_3$ heterostructures with high visible light efficiency in photocatalytic degradation of pollutants, *Adv. Mater.* 26 (2014) 892–898.

[38] S. Juntrapirom, D. Tantravivat, S. Suntalelat, O. Thongsook, S. Phanichphant, B. Inceesungvorn, Visible light photocatalytic performance and mechanism of highly efficient SnS/BiOI heterojunction, *J. Colloid Interface Sci.* 504 (2017) 711–720.

[39] H. Guo, T. Ke, N. Gao, Y. Liu, X. Cheng, Enhanced degradation of aqueous norfloxacin and enrofloxacin by UV-activated persulfate: kinetics, pathways and deactivation, *Chem. Eng. J.* 316 (2017) 471–480.

[40] B. Yang, R.S. Kookana, M. Williams, G.-G. Ying, J. Du, H. Doan, A. Kumar, Oxidation of ciprofloxacin and enrofloxacin by ferrate (VI): Products identification, and toxicity evaluation, *J. Hazard. Mater.* 320 (2016) 296–303.

[41] C. Guo, S. Gao, J. Lv, S. Hou, Y. Zhang, J. Xu, Assessing the photocatalytic transformation of norfloxacin by BiOBr /iron oxides hybrid photocatalyst: kinetics, intermediates, and influencing factors, *Appl. Catal. B* 205 (2017) 68–77.

[42] D.H. Ding, C. Liu, Y.F. Ji, Q. Yang, L.L. Chen, C.L. Jiang, T.M. Cai, Mechanism insight of degradation of norfloxacin by magnetite nanoparticles activated persulfate: identification of radicals and degradation pathway, *Chem. Eng. J.* 308 (2017) 330–339.

[43] N. Shao, J.N. Wang, D.D. Wang, P. Corvini, Preparation of three-dimensional $\text{Ag}_3\text{PO}_4/\text{TiO}_2@\text{MoS}_2$ for enhanced visible-light photocatalytic activity and anti-potocorrosion, *Appl. Catal. B* 203 (2017) 964–978.

[44] S.N. Yin, T. Yao, T.H. Wu, Y. Zhang, P. Wang, Novel metal nanoparticle-enhanced fluorescence for determination of trace amounts of fluoroquinolone in aqueous solutions, *Talanta* 174 (2017) 14–20.

[45] W. Chen, P. Westerhoff, J.A. Leenheer, K. Booksh, Fluorescence excitation – emission matrix regional integration to quantify spectra for dissolved organic matter, *Environ. Sci. Technol.* 37 (2003) 5701–5710.

[46] X.J. Wen, C.G. Niu, L. Zhang, D.W. Huang, G.M. Zeng, In-situ synthesis of visible-light-driven plasmonic $\text{Ag}/\text{AgCl}-\text{CdWO}_4$ photocatalyst, *Ceram. Int.* 43 (2017) 1922–1929.

[47] S.F. Yang, C.G. Niu, D.W. Huang, H. Zhang, C. Liang, G.M. Zeng, SrTiO_3 nanocubes decorated with Ag/AgCl nanoparticles as photocatalysts with enhanced visible-light photocatalytic activity towards the degradation of dyes, phenol and bisphenol A, *Environ. Sci. Nano* 4 (2017) 585–595.

[48] C. Liang, C.G. Niu, X.J. Wen, S.F. Yang, M.C. Shen, G.M. Zeng, Effective removal of colourless pollutants and organic dyes by $\text{Ag}@\text{AgCl}$ nanoparticle-modified $\text{CaSn}(\text{OH})_6$ composite under visible light irradiation, *New J. Chem.* 41 (2017) 5334–5346.

[49] X.J. Wen, C. Zhang, C.G. Niu, L. Zhang, D.W. Huang, X.Y. Wang, X.G. Zhang, G.M. Zeng, Facile synthesis of a visible light $\text{Fe}_2\text{O}_3/\text{BiOBr}$ composite with high photocatalytic performance, *RSC Adv.* 6 (2016) 4035–4042.

[50] X.J. Wen, C.G. Niu, D.W. Huang, L. Zhang, C. Liang, G.M. Zeng, Study on photocatalytic degradation pathway of norfloxacin and mineralization activity using a novel ternary $\text{Ag}/\text{AgCl}-\text{CeO}_2$ photocatalyst, *J. Catal.* (2017), <http://dx.doi.org/10.1016/j.jcat.2017.08.028>.

[51] X.J. Wen, C.G. Niu, L. Zhang, G.M. Zeng, Fabrication of SnO_2 nanoparticles/ BiOI n–p heterostructure for wider spectrum visible-light photocatalytic degradation of antibiotic oxytetracycline hydrochloride, *ACS Sustain. Chem. Eng.* 5 (2017) 5134–5147.

[52] J. Di, J. Xia, Y. Ge, L. Xu, H. Xu, J. Chen, M. He, H. Li, Facile fabrication and enhanced visible light photocatalytic activity of few-layer MoS_2 coupled BiOBr microspheres, *Dalton Trans.* 43 (2014) 15429–15438.

[53] A.W. Bott, Electrochemistry of semiconductors, *Curr. Sep.* 17 (1998) 87–92.

[54] J. Ke, J. Liu, H. Sun, H. Zhang, X. Duan, P. Liang, X. Li, M.O. Tade, S. Liu, S. Wang, Facile assembly of $\text{Bi}_2\text{O}_3/\text{Bi}_2\text{S}_3/\text{MoS}_2$ np heterojunction with layered n– Bi_2O_3 and p– MoS_2 for enhanced photocatalytic water oxidation and pollutant degradation, *Appl. Catal. B* 200 (2017) 47–55.

[55] F. Meng, J. Li, S.K. Cushing, M. Zhi, N. Wu, Solar hydrogen generation by nanoscale p–n junction of p-type molybdenum disulfide/n-type nitrogen-doped reduced graphene oxide, *J. Am. Chem. Soc.* 135 (2013) 10286–10289.

[56] L. Wu, S. Fang, L. Ge, C. Han, P. Qiu, Y. Xin, Facile synthesis of $\text{Ag}@\text{CeO}_2$ core–shell plasmonic photocatalysts with enhanced visible-light photocatalytic performance, *J. Hazard. Mater.* 300 (2015) 93–103.

[57] S. Linic, P. Christopher, D.B. Ingram, Plasmonic–metal nanostructures for efficient conversion of solar to chemical energy, *Nat. Mater.* 10 (2011) 911.

[58] E. Kraut, R. Grant, J. Waldrop, S. Kowalczyk, Precise determination of the valence-band edge in X-ray photoemission spectra: application to measurement of semiconductor interface potentials, *Phys. Rev. Lett.* 44 (1980) 1620.

[59] L. Liu, W. Yang, W. Sun, Q. Li, J.K. Shang, Creation of $\text{Cu}_2\text{O}@\text{TiO}_2$ composite photocatalysts with p–n heterojunctions formed on exposed Cu_2O facets, their energy band alignment study, and their enhanced photocatalytic activity under illumination with visible light, *ACS Appl. Mater. Interfaces* 7 (2015) 1465–1476.

[60] M.T. Uddin, Y. Nicolas, C. Olivier, T. Toupance, L. Servant, M.M. Müller, H.J. Klebe, Jürgen Ziegler, W. Jaegermann, Nanostructured SnO_2-ZnO heterojunction photocatalysts showing enhanced photocatalytic activity for the degradation of organic dyes, *Inorg. Chem.* 51 (2012) 7764–7773.